

Article

Spark Plasma Sintering (SPS) of Multi-Principal Element Alloys of Copper-Niobium-Titanium-Di-Boride-Graphite, Investigation of Microstructures, and Properties

Azunna Agwo Eze ^{1,*}, Emmanuel Rotimi Sadiku ¹, Williams Kehinde Kupolati ², Jacques Snyman ², Julius Musyoka Ndambuki ² and Idowu David Ibrahim ¹

¹ Institute for NanoEngineering Research (INER), Department of Chemical, Metallurgy and Materials Engineering, Tshwane University of Technology, Pretoria 0001, South Africa

² Department of Civil Engineering, Tshwane University of Technology, Pretoria 0001, South Africa

* Correspondence: ezeaaben@gmail.com

Abstract: A near-equiatomic multi-principal element alloy of $\text{Cu}_{40}\text{Nb}_{30}(\text{TiB}_2)_{20}\text{C}_{10}$ with both nano-particle size (14 nm) and micron-particle sizes ($\sim 44 \mu\text{m}$) of Nb was designed and made via the spark plasma sintering technique at two different sintered temperatures of 650 °C and 700 °C with other SPS parameters being constant. The sintering mode, microstructures, microhardness, density, relative density, wear behavior, and corrosion properties of the alloys were investigated and compared to ascertain the best for aerospace applications. The SPS technique was applied to produce the tested samples in this study. The results showed that the alloys with nano-particles of Nb sintered faster, with the lowest wear rate, and their microstructure shows a dendritic configuration with the existence of graphite-rich and niobium-rich nano-segregations in the inter-dendritic areas with the lowest coefficient of friction, $\text{Cu-NbTiB}_2\text{C}$ with nano-particles of Nb sintered at 650 °C recorded the highest microhardness value (786.03 $\text{HV}_{0.2}$), and $\text{CuNbTiB}_2\text{C}$ with micro-particles of Nb sintered at 700 °C exhibited the best anti-corrosion characteristics in a sulphuric acid environment. The results obtained in this study correspond to the requirements for high-performance engineering materials, which will make the novel materials relevant in the aerospace industry.

Keywords: spark plasma sintering; $\text{Cu-Nb-TiB}_2\text{-C}$; sintering mechanisms; microstructure; wear and corrosion



Citation: Eze, A.A.; Sadiku, E.R.; Kupolati, W.K.; Snyman, J.; Ndambuki, J.M.; Ibrahim, I.D. Spark Plasma Sintering (SPS) of Multi-Principal Element Alloys of Copper-Niobium-Titanium-Di-Boride-Graphite, Investigation of Microstructures, and Properties. *Crystals* **2022**, *12*, 1754. <https://doi.org/10.3390/cryst12121754>

Academic Editors: Yufei Zu, Huifang Pang and Fan Wu

Received: 15 October 2022
Accepted: 29 November 2022
Published: 3 December 2022

Publisher's Note: MDPI stays neutral with regard to jurisdictional claims in published maps and institutional affiliations.



Copyright: © 2022 by the authors. Licensee MDPI, Basel, Switzerland. This article is an open access article distributed under the terms and conditions of the Creative Commons Attribution (CC BY) license (<https://creativecommons.org/licenses/by/4.0/>).

1. Introduction

There is an intense search to design structural materials that can live through the extensive harsh and severe conditions of performance, and this will be of great importance to the upcoming generation of energy and aerospace technologies. The recent emphasis has been on multi-principal element alloys that are recently enjoying fast progress with a high level of effort regarding the design of novel alloy structures for possible uses in several industries, including die and mold materials for high temperatures, thermal bond coating spray, turbine blades, radiation-resistant materials, and renewable energy fabrication [1–8]. Conventional alloys will not meet the expected basic structural properties that are required in draconian conditions of applications at all times. The families of conventional alloys emphasize exploiting one principal element with minor amounts of other elements to improve the properties of the material. However, well-selected and designed multi-principal element alloys, which are solid-solution phases with four or more other major elements on simple core lattices, are anticipated to meet the more rudimentary structural requirements in draconian conditions than conventional alloys. The exceptional microstructures of multi-principal element alloys and their outstanding chemical and physical properties have attracted the attention of advanced material researchers all over the world [3]. The earliest and most intensely investigated alloy systems are the 3d block

transition metal multi-principal element alloys that are built on the following elements: Copper, titanium, chromium, iron, zinc, nickel, cobalt, manganese, and vanadium [3]. Another important multi-principal element alloy system is a refractory metal multi-principal element alloy system with high strength and melting temperatures greater than 1800 °C containing the elements niobium, chromium, vanadium, molybdenum, hafnium, tungsten, and tantalum [3]. The combination of refractory metals with elements known for enhancing oxidation resistance, high-temperature strength, and thermal stability makes them ideal candidates for high-temperature applications. Niobium and titanium are among the prime candidates as structural materials for advanced aerospace vehicles and flight propulsion systems. Unlike conventional alloys, multi-principle element alloys employ the approach of using multiple elements in equiatomic or near-equiatomic proportions [9]. This conception was first recommended by two different groups of researchers, Yeh et al. (2004) and Cantor et al. (2004) [10,11]. These multi-principal element alloys formed steady solid solutions, which were credited to their high compositional entropies of mixing [9]. The two studies established the nonexistence of multipart phases and microstructures, which inspired the further expansion of new multi-principal element alloys [9]. The concept of joining refractory metals within such alloys was later proven practical in molybdenum-niobium-tantalum-nickel and molybdenum-niobium-tantalum-vanadium-tungsten multi-principal element alloys [12]. The aim was to construct alloys appropriate for use in areas that needed high strength at high-temperatures operation, including those in the aerospace industries and energy industries. The amalgamation of high melting temperature, creep resistance, and oxidation resistance, particularly in the temperature range above 8300 °C, brand the refractory metals noble nominee materials for high-temperature utilization [13]. Recently, many research works have called attention to the excellent corrosion resistance exhibited by the synthetic multi-principal element alloy [14–16]. The integration of titanium into multi-principal element alloy is also imperative owing to their low-density advantages, high specific strength, and outstanding corrosion resistance, as well as biocompatibility nature. Titanium alloys are extensively used in several areas including the aviation industry, navigation, and biomedicine industries [17]. However, the reason for having weak oxidation resistance at temperatures higher than 600 °C in addition to the inadequate anti-wear capacity, the wider usage of titanium alloys is narrowed [17].

The fabrication of multi-principal element alloys with preferred microstructures and properties using conventional manufacturing techniques similar to casting is still challenging [3]. Another fabrication technique that has been used to produce multi-principal element alloys is additive manufacturing [3], but the strength of additive manufactured material is still inferior and has a poor surface finish compared to that of other fabrication techniques [18]. The fabrication of multi-principal element alloys with tailorable microstructures and excellent mechanical properties has become possible through the use of SPS techniques, which were applied in this study. This was made possible through the sintering of the alloys in a short period at temperatures below the respective melting temperatures of the constituent elements of the alloys. The advantage of the SPS means of production in this study is that it helps and prohibits the immiscibility difficulties met when casting melted multi-principal element alloys.

In this study, a multi-principal alloy with a near-equiatomic composition of elements of copper, niobium, titanium, di-boride, and graphite (40% weight of Cu, 30% weight of Nb, 20% weight of Ti B₂, and 10% weight of C) was produced via the powder metallurgy route with the help of the spark plasma sintering technique. Their sintering mechanisms, microstructures, microhardness, wear, and corrosion properties were investigated. Moreover, there is no literature work found on multi-principal element alloys except in this study, and this is a first-hand study of the alloy.

2. Materials and Methods

2.1. Materials

The powders of copper, niobium (nano and micron particle sizes), titanium-diboride, and graphite were selected for the investigation. All the materials were supplied by Alfa Aesar. Table 1 contained the chemical composition of the selected materials.

Table 1. Chemical composition of the multi-principal alloy and Spark Plasma Sintering parameters with sintering dies.

Constituent Element	Weight Percent (wt.%)		Purity (%)	Particle Size	
Copper, Cu	40		99	44 μm	
Niobium, Nb	30		99.9	14 nm–44 μm	
Titanium diboride, TiB_2	20		99	75 μm	
Graphite, C	10		99.8	14.43 nm	
Spark plasma sintering parameters					
Alloys	Sintering temperature ($^{\circ}\text{C}$)		Pressure (MPa)	Heating rate ($^{\circ}\text{C}/\text{min}$)	Holding time (min)
Cu-Nb(nano)- TiB_2 -G	650	700	60	50	5
Cu-Nb(micron)- TiB_2 -G	650	700	60	50	5
Sintering dies	Diameter (mm)		Height (mm)		Volume ($=\pi r^2 h$) (mm^3)
Graphite dies	30		5		3534.29

2.2. Methods

2.2.1. Powder Mixing and Sintering Process

The starting materials were used to design multi-principal alloys of $\text{Cu}_{40}\text{-Nb}(\text{nano})_{30}\text{-(TiB}_2\text{)}_{20}\text{-C}_{10}$ and $\text{Cu}_{40}\text{-Nb}(\text{micron})_{30}\text{-(TiB}_2\text{)}_{20}\text{-C}_{10}$. The powders of each of these alloys were separately inserted in the plastic bottle with steel balls with a diameter of 0.4 mm at a ball-to-powder ratio of 1:1 to help reduce the rate of powder agglomeration and were further mixed using a tubular mixer machine for six hours at a speed of 72 rev./min. After mixing the powders, the steel balls were removed from the admixed powders, before being sintered, using the FCT system GmbH- FCT group spark plasma sintering machine with an ON/OFF pulse direct electrical current. The sintering of each sample was performed at two different sintering temperatures of 650 $^{\circ}\text{C}$ and 700 $^{\circ}\text{C}$ in an argon atmosphere at a heating rate of 50 $^{\circ}\text{C}/\text{min}$, applied pressure of 50 MPa, dwelling time of 5 min, input power supply of 456.5 VAC, and cycling of 50 H. The mold used to obtain the differently sintered spacemen was graphite dies with a diameter of 30 mm and a height of 5 mm. Detailed information for the spark plasma sintering process of the alloys is contained in Table 1.

2.2.2. Micro-Hardness Test

The microhardness was measured using the Vickers indentation method, at an applied load of 100 Kg force, with a holding time of 5 s, and the test result for each sample was the arithmetic mean of six (6) successive indentations with standard deviations.

2.2.3. Microstructure Test

A JSM 7600F Joel ultra-high-resolution field emission scanning electron microscope incorporated with energy-dispersive X-ray spectroscopy was used for the microscopy studies of the sintered alloys.

2.2.4. Wear Test

The wear behavior of the sintered multi-principal element alloy was tested using Anton-Paartribometer TRB3 version 8.1.8, which was provided with a computer-controlled pin-on-disc arrangement operated at room temperature. During the test, a normal load of

20 N was applied at a frequency of 15 Hz, and the coefficient of friction as a function of sliding time was investigated.

2.2.5. Corrosion Test

The corrosion study of the sintered multi-principal element alloys was carried out in a container that enclosed a mole of sulphuric (H_2SO_4) acid solution that acted as an environment, with each tested sample as the working electrode and the graphite rod as a counter electrode and reference electrode (saturated silver/silver chloride). It was further carried out with VersaSTAT 4 with versa studio version 4.9 software. The potentiodynamic polarization procedure was used to review the general electrochemical behavior of the sintered multi-principal element alloys. However, before scanning, each one of the tested samples was immersed in the electrolyte for approximately 6 min to permit them to become stable before the open circuit potential measurement, which was performed for 2 h. Every one of the samples tested was scanned at a scan rate of 0.002 Volts per second with a potential variety from -1.5 to $+1.5$ volts.

3. Results and Discussions

3.1. Sintering Mode of $CuNbTiB_2C$ Multi-Principal Element Alloys

Figure 1 summarizes the sintering mode that occurred during the sintering of the $CuNbTiB_2C$ multi-principal element alloys. It shows the shrinkage of the particles versus the sintering temperatures during the SPS of the alloys. These revealed how the shrinkage of the punch exerted a uniaxial force on the sintering powder with the increase in the sintering temperatures during the sintering of the multi-principal alloys. The shrinkage of the axial punch on the sintering powders decreases as the temperature increases from 250 °C to the final sintering temperatures of 650 °C and 700 °C. The $CuNbTiB_2C$ alloy with micro-particle of Nb sintered at final temperatures of 650 °C and 700 °C was seen to have the most dramatic increase in the shrinkage of their particles beyond the sintering temperature of 400 °C and declined after a temperature of approximately 550 °C. What happened in the curves of Figure 1 between temperatures of 400 °C and 500 °C may be where there are local deformations of the particles, while the region between 500 °C and 600 °C is where there are bulk deformations of the particles. The observation above is in line with the work of Diouf and Molinari (2012) [19]. The researchers studied the deformation mechanism of copper powders in spark plasma sintering where they demonstrated that the local deformation of copper occurred at a temperature between 200 °C and 500 °C and changed to bulk deformation at temperatures above 500 °C [19].

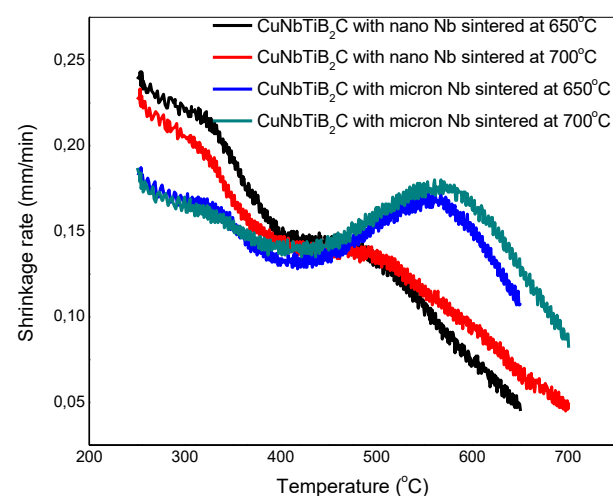


Figure 1. Shrinkage rate of the particles versus sintering temperatures during the SPS of the alloys.

The $CuNbTiB_2C$ alloy with nano-particles of Nb sintered at 650 °C recorded the largest particle shrinkage, which decreased as the final sintering temperatures were approaching.

It was followed by the CuNbTiB₂C alloy with nano-particles of Nb sintered at 700 °C. The pattern of sintering mode that took place in the CuNbTiB₂C with nano-particles of Nb was alike in both sintered temperatures of 650 °C and 700 °C. The CuNbTiB₂C alloy with micro-particles of Nb, on the other hand, maintained the same pattern of the sintering mode in both 650 °C and 700 °C sintered temperatures. The alloys with nano-particles of Nb showed a different pattern in their sintering mode when compared with CuNbTiB₂C alloys with micro-particles of Nb. The dichotomy observed is a result of differences in the particle sizes of their constituent elements. The nano-particle sizes of Niobium and Graphite in the alloys could not restrict the uniaxial pressure of the pressing tool, and the absorption of more heat was improved, which softens the particles as the temperature increased. The incidence is the attribute of the powdered materials becoming softer as the temperatures increases.

However, mechanical, thermal, and electrical effects are the three impacts that made up the sintering mode during SPS of these CuNbTiB₂C multi-principal element alloys. The exertion of pressure on the powders during the SPS helped the particles of the sintering powders to rearrange and improve their consolidation at low temperatures and enhanced their microstructures as well as mechanical properties. When the temperature became higher, further densification would be boosted via the control creep law (i.e., the samples turn out to be softer at higher sintering temperatures, which were more on the nano-particles). During the sintering, the thermal effect plays a vital role and the speedy heating rates increase densification and improved the microstructures. The EDS graph results in Figures 2 and 3 showed no contaminations after sintering. This resulted in the fine microstructures that were obtained as can be seen in Figures 4 and 5. These are the attributes of the fast heating rate and short sintering time properties of the spark plasma sintering technique, which do not allow contamination between the spacemen and the sintering dies. The ON and OFF direct current (DC) pulse engenders the electrical influence that can be distinguished in the field and current influences [20]. Therefore, the resulting microstructures shown in Figures 4 and 5 were expected to be influenced by the interconnection between the samples' particles and electrical current. The particles of the admixed samples could be electrically isolating or conducting, which might have resulted in diverse electrical influences. For the conducting particles, current flows through the admixed powders of the multi-principal element alloys, and heat is created through Joule heating and transferred to the admixed powders via conduction [21]. Thus, the sintering mechanism determined the nature of the microstructure the alloy would have after being sintered.

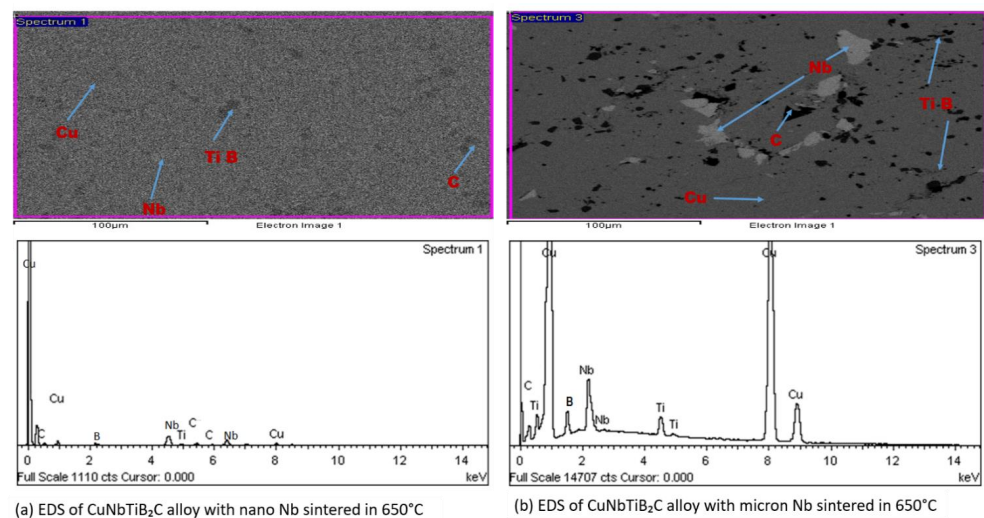


Figure 2. (a,b) compare the EDS graph, of CuNbTiB₂C alloys with nano and micron both sintered at 650 °C.

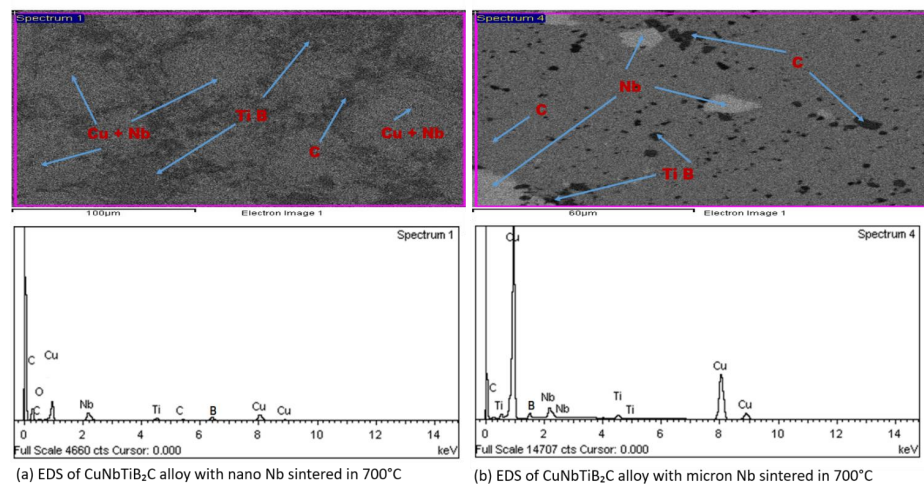


Figure 3. (a,b) compare the EDS graph of CuNbTiB₂C alloys with nano and micron both sintered at 700 °C.

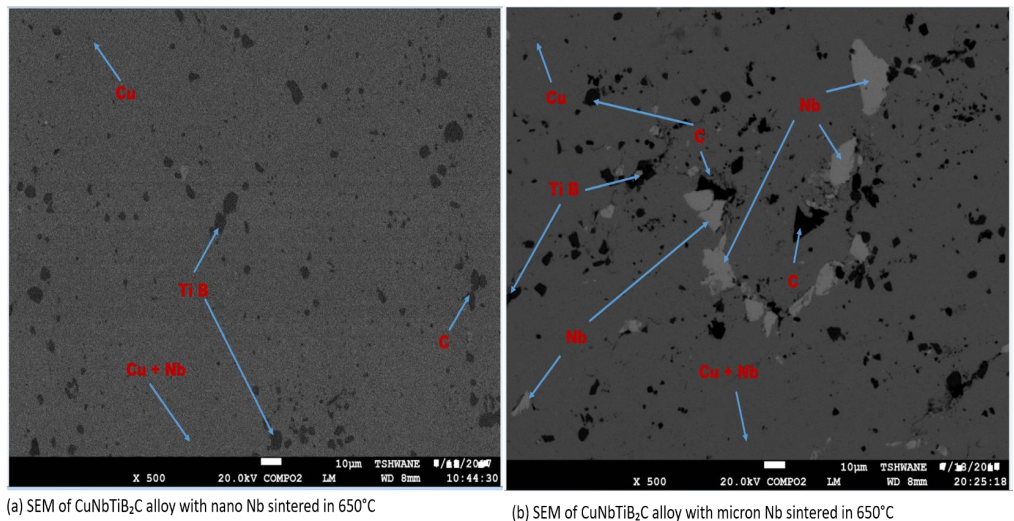


Figure 4. (a,b) compare the SEM of CuNbTiB₂C alloys with nano and micron both sintered at 650 °C.

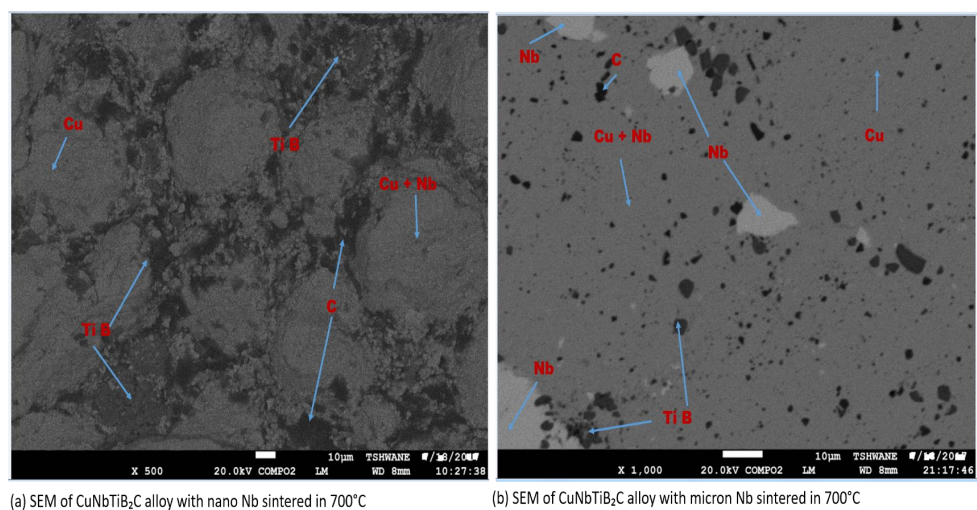


Figure 5. (a,b) compare the SEM of CuNbTiB₂C alloys with nano and micron both sintered at 700 °C.

3.2. EDS Analysis, SEM, and Micro-Hardness, Density, and Relative Density of the Sintered Multi-Principal Element Alloys

Figures 2–5 display the EDS analysis and SEM images of the sintered CuNbTiB₂C multi-principal element alloys sintered at 650 °C and 700 °C. Figure 2a,b compare the EDS graphs of CuNbTiB₂C alloys with nano-particles and micro-particles of Nb sintered at 650 °C, while Figure 3a,b compare the EDS graphs of CuNbTiB₂C alloys with nano-particles and micro-particles of Nb sintered at 700 °C. Figure 4a,b compare the SEM of CuNbTiB₂C alloys with nano and micro-particles of Nb sintered at 650 °C, while Figure 5a,b compare the SEM of CuNbTiB₂C alloys with nano-particles and micro-particles of Nb sintered at 700 °C. At these sintered temperatures (650 °C and 700 °C), the resulting EDS graphs showed that the multi-principal element alloys still retained their purities after their admixed powders were sintered. It was only in the alloy of CuNbTiB₂C with nano-particles of Nb sintered at 700 °C that a trace of oxygen was found (Figure 3a). The presence of oxygen in the alloy (Figure 3a) indicated the presence of pores in the microstructure of that particular alloy (Figure 5a). However, the microstructures of other alloys showed no pores as no oxygen was found in their EDS graphs. The microstructure of the CuNbTiB₂C alloy with nano-particles of Nb sintered at 700 °C (Figure 5a) shows the agglomeration of particles. This could be attributed to the nano-particles that were not evenly dispersed during the mixing of the powders, which might be the cause of the pores that evolved after sintering. In Figure 5a, the microstructure also shows a dendritic arrangement with the existence of graphite-rich and niobium-rich nano-segregations in the inter-dendritic areas. The microstructure of CuNbTiB₂C with nano-particles of Nb sintered at 650 °C is seen to be more homogenous and denser as compared to others. The whitish pigments found in each of the microstructures are the concentrations of niobium (Nb) particles, while the black pigments are mostly the presence of titanium di-boride (TiB₂) particles and graphite (C) particles and the brownish pigments of copper (Cu) could not have reflected but their particles were evenly dispersed in the microstructures of the alloys. The powder mixing and SPS mode in Figure 1 have a great influence on the nature of the microstructures that were obtained. The nature of microstructures in each of the alloys also determines their properties.

Table 2 contains the values of microhardness, density, and relative density for the sintered specimens. In Table 2, the alloy of CuNbTiB₂C with nano-particles of Nb sintered at 650 °C recorded the highest microhardness value of 786.03 HV, followed by an alloy of CuNbTiB₂C with micro-particles of Nb sintered at 650 °C, which recorded a microhardness value of 754.16 HV. The alloy of CuNbTiB₂C with micro-particles of Nb sintered at 700 °C recorded a microhardness value of 745.06 HV, and the alloy of CuNbTiB₂C with nano-particles of Nb sintered at 700 °C recorded the lowest microhardness value of 734.50 HV. The high microhardness value recorded by an alloy of CuNbTiB₂C with nano-particles of Nb sintered at 650 °C may be due to the strong interfacial bonding among the constituent elements of the alloy. An alloy of CuNbTiB₂C with micro-particles of Nb sintered at 650 °C recorded the highest density value of 7.806 g/cm³ and a relative density of 96%, which was followed by an alloy of CuNbTiB₂C with micro-particles of Nb sintered at 700 °C that recorded a density value of 7.758 g/cm³ and a relative density of 95%. An alloy of CuNbTiB₂C with nano-particles of Nb sintered at 700 °C recorded a density of 7.390 g/cm³ and a relative density of 91%, and lastly, an alloy of CuNbTiB₂C with nano-particles of Nb sintered at 650 °C recorded the lowest density of 7.309 g/cm³ with a relative density of 90%. The high-density value recorded by an alloy of CuNbTiB₂C with micro-particles of Nb sintered at 650 °C may be a result of the acceleration of copper and niobium, which have high density.

Table 2. Summary of the micro-hardness, density, and relative density of the sintered alloys.

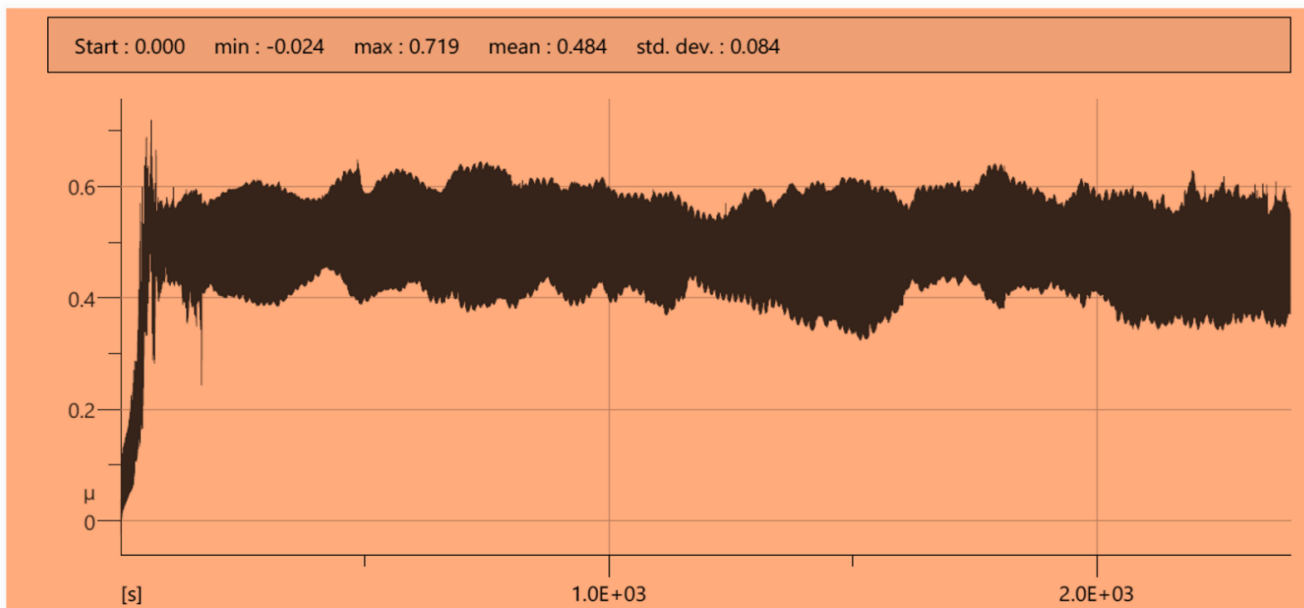
Multi-Principal Element Alloys	Micro-Hardness (HV _{0.2})	Density (g/cm ³)	Relative Density (%)
CuNbTiB ₂ C with nano-particles of Nb sintered at 650 °C	786.03	7.309	90
CuNbTiB ₂ C with nano-particles of Nb sintered at 700 °C	734.50	7.390	91
CuNbTiB ₂ C with micro-particles of Nb sintered at 650 °C	754.16	7.806	96
CuNbTiB ₂ C with micro-particles of Nb sintered at 700 °C	745.06	7.758	95

3.3. Wear Behavior of the Sintered Multi-Principal Element Alloys

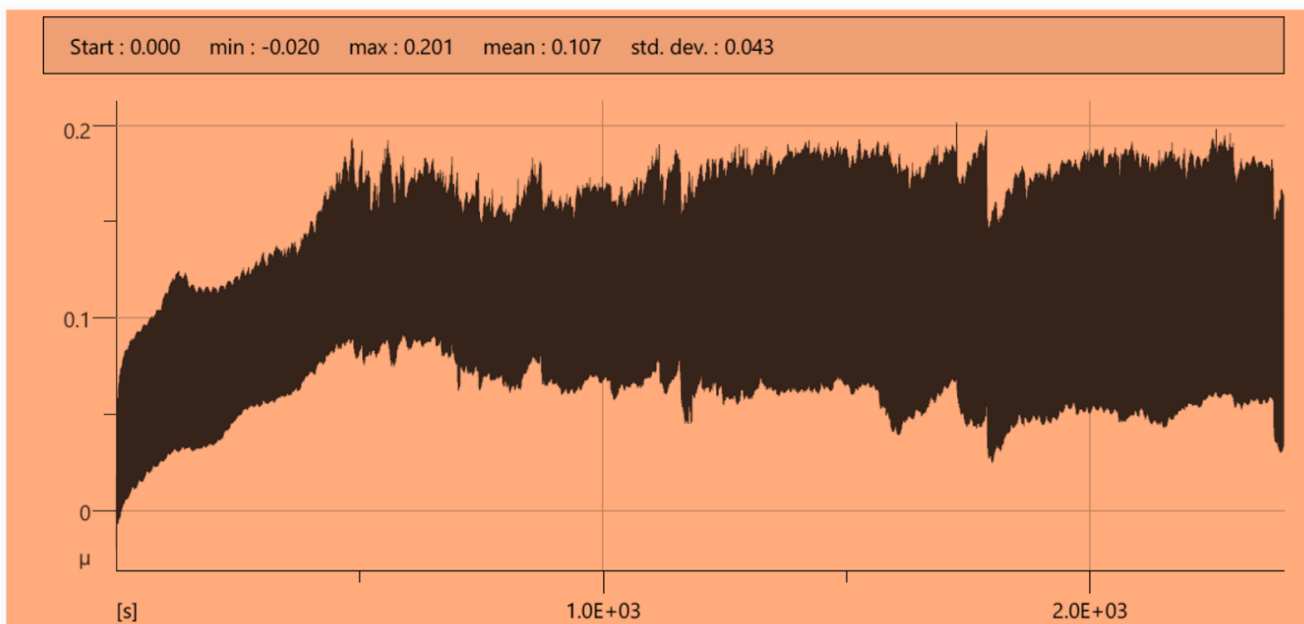
The coefficient of friction, μ , against sliding time and t for all the multi-principal alloys under the same applied load of 20 N are reported in Figures 6 and 7, respectively, and was summarized in Table 3. Figure 6a,b show the graphs of the coefficient of friction versus time of CuNbTiB₂C alloys with nano-particles and micro-particles of Nb both sintered at 650 °C. Figure 7a,b show the graphs of the coefficient of friction versus time of CuNbTiB₂C alloys with nano-particle and micro-particles of Nb both sintered at 700 °C. The alloy of CuNbTiB₂C with micro-particles of Nb sintered at 650 °C recorded the lowest coefficient of friction with a maximum value of 0.201 compared to other alloys. This might be due to the presence of the micron-particle sizes, which might not have permitted much flow of heat into the alloy and the low sintering temperature that could not have supported many triggers of Ti particles. The frictional behavior of CuNbTiB₂C with nano-particles of Nb sintered at 700 °C is seen to be steady compared to other alloys, while that of the CuNbTiB₂C alloy with micro-particle of Nb sintered at 700 °C (Figure 7b) exhibited high fluctuation compared to other alloys. This could mean that there was a modification that took place on the surface of the alloy during the sliding. However, the dissimilarity in the definite wear rate and the coefficient of frictional behavior of these alloys could also be attributed to the interchange between the surfaces in the sequence of the sliding. The observed fluctuation could be mostly due to the modifications that took place throughout the sliding. In particular, some of the harshness is transferred from the specimen surface to the counter-face surface or the conflicts are controlled by the set-off parameters, contract positions, and the hardness of the material [22]. Once there are materials transferred from one surface to another surface and detachments have occurred, these would lead to fluctuations in the coefficient of friction. However, some researchers have tried to correlate the wear and friction behavior of materials altogether [23]. There is a small number of authors who have accepted that there is a correlation between the wear and frictional conduct of materials, specifically high frictional coefficients constitute high resistance in the interface, which results in superior wear behavior [24]. At present, a greater number of researchers have accepted that wear is a response to the rubbing system, which is independent of the frictional performance [24]. Therefore, following the idea that the high frictional coefficients constitute high resistance in the interface, it then means that CuNbTiB₂C with nano-particles of Nb sintered at 650 °C (Figure 6a) has a superior wear behavior over the rest of the multi-principal element alloys in this study.

Table 3. Summary of the wear behavior of the produced multi-principal element alloys.

Multi-Principal Element Alloys	Minimum Coefficient of Friction, μ	Maximum Coefficient of Friction, μ	Mean Value of μ	Standard Deviation Value of μ
CuNbTiB ₂ C with nano-particle of Nb sintered at 650 °C	−0.024	0.719	0.484	0.084
CuNbTiB ₂ C with nano-particles of Nb sintered at 700 °C	−0.044	0.416	0.286	0.065
CuNbTiB ₂ C with micro-particles of Nb sintered at 650 °C	−0.020	0.201	0.107	0.043
CuNbTiB ₂ C with micro-particles of Nb sintered at 700 °C	−0.171	0.425	0.177	0.097



(a) CuNbTiB₂C alloy with nano Nb sintered in 650°C



(b) CuNbTiB₂C alloy with micron Nb sintered in 650°C

Figure 6. (a,b) compare the graph of the coefficient of friction versus time of CuNbTiB₂C alloys with nano and micron both sintered at 650 °C.

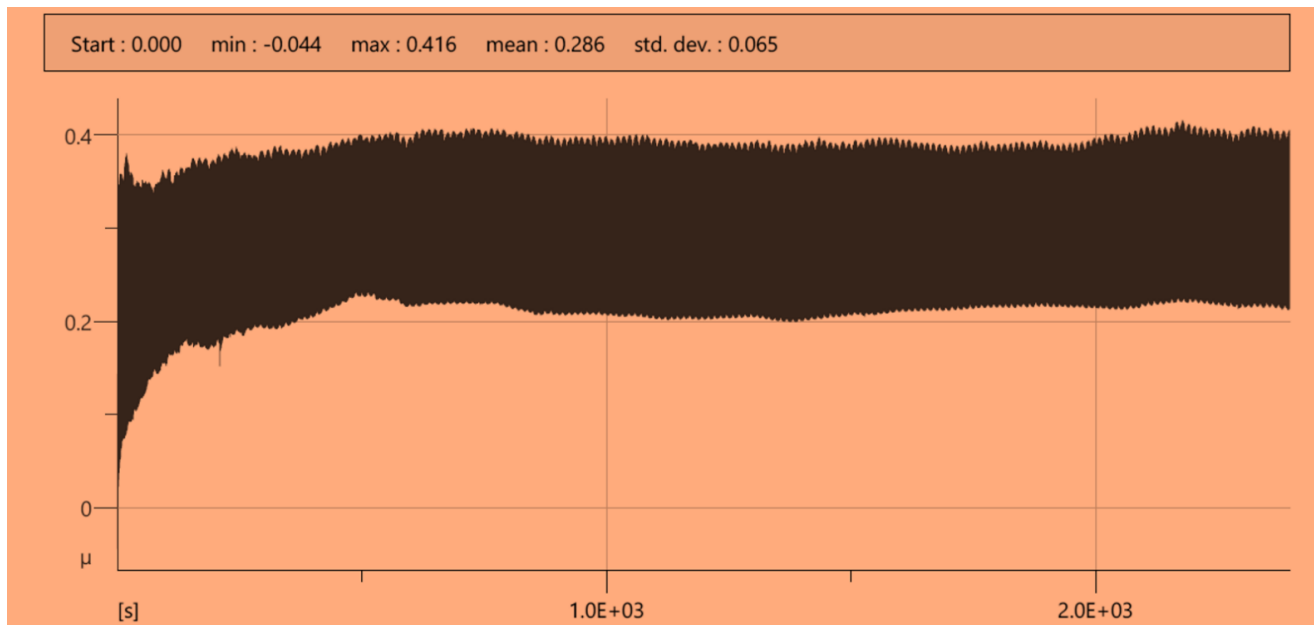
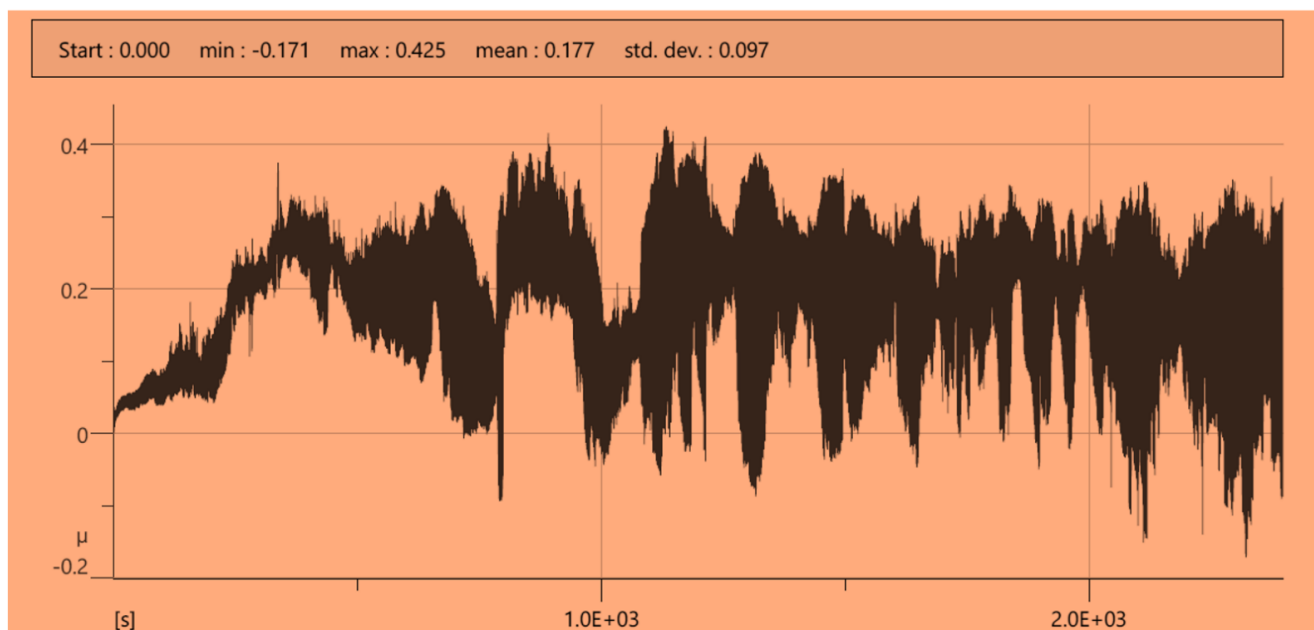
(a) CuNbTiB₂C alloy with nano Nb sintered in 700°C(b) CuNbTiB₂C alloy with micron Nb sintered in 700°C

Figure 7. (a,b) compare the graph of the coefficient of friction versus time of CuNbTiB₂C alloys with nano and micron both sintered at 700 °C.

3.4. Corrosion Performance of the Multi-Principal Element Alloys of CuNbTiB₂C

Figure 8 shows the comparison of potentiodynamic polarization curves of the novel multi-principal element alloys of CuNbTiB₂C in 1-mole H₂SO₄ acid. The potentiodynamic polarization methodology was applied to ascertain any likelihood of the produced CuNbTiB₂C multi-principal element alloys to passivity. The passivation potentiality is the electrochemical possibility through which the passivation of the alloy occurs. Hence, it is observable that the lower the amount of this potential, the greater the corrosion protection (resistance) of the produced multi-principal alloy. The passivation capacity is reliant not only on the electrochemical potential but also on the analytical passivation current density [25]. The lower the current density exists, the simple the unconstrained passivation due

to oxygen arises. However, in Figure 8, the potentiodynamic polarization curve revealed that the multi-principal element alloy of $\text{CuNbTiB}_2\text{C}$ with micro-particles of Nb sintered at 700°C shows the preeminent corrosion resistance out of all the alloys. It was triggered by the lowest measured values of I_{corr} and E_{corr} , and the graph in Figure 8 seemingly shows its resistance in a 1-mole solution of sulphuric acid (H_2SO_4). Multi-principal element alloys of $\text{CuNbTiB}_2\text{C}$ with nano-particles of Nb sintered at 650°C and $\text{CuNbTiB}_2\text{C}$ with micro-particles of Nb sintered at 650°C showed similar behavior in this acidic environment, and they showed good anti-corrosion properties in the environment of sulphuric acid. The third highest corrosion resistance in this acidic environment is the multi-principal element alloy of $\text{CuNbTiB}_2\text{C}$ with nano-particles of Nb sintered at 700°C . It shows the worst results and considerably degraded the sulphuric acid environment. The scenario could be attributed to the nature of its microstructure (Figure 5a), which indicated the presence of pores on the alloy and could serve as the corrosion site. It was confirmed in the EDS graph of the alloy, which shows the presence of oxygen (Figure 3a). The corrosion site (pores) on the alloy could be attributed to the formation of weak interfacial bonds among the constituent elements of the alloy. Furthermore, the pores might be initiated at the area of the matrix interface and could be the site for corrosion. However, most metal matrix composites always initiate a chemical or physical heterogeneity such as the reinforcement interface, defect, inter-metallic, mechanically damaged region, grain boundary, inclusion, or dislocation [26,27].

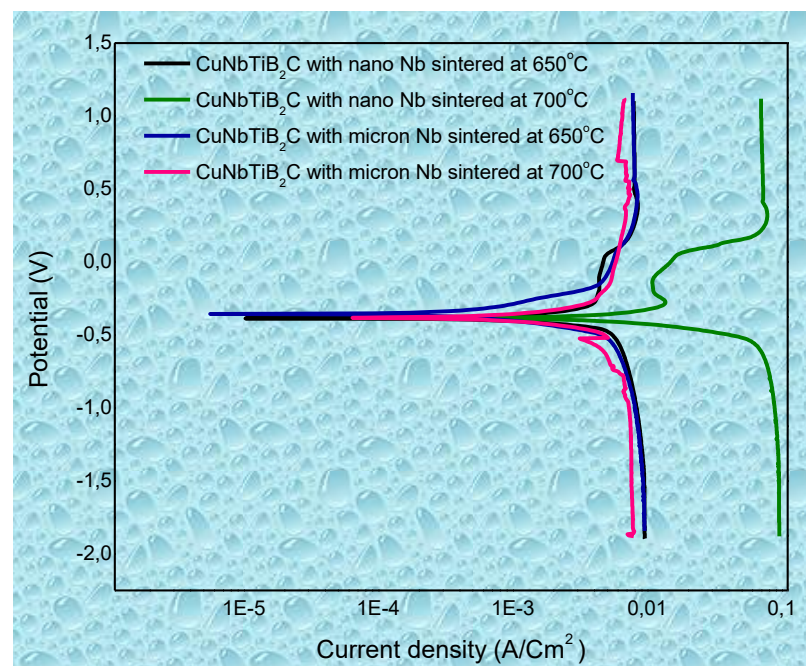


Figure 8. Shows the comparison of the potentiodynamic polarization curve of the novel multi-principal alloys of $\text{CuNbTiB}_2\text{C}$ in 1 mole H_2SO_4 acid.

The good anti-corrosion properties exhibited by the multi-principal element alloys of $\text{CuNbTiB}_2\text{C}$ with micro-particles of Nb sintered at both 650°C and 700°C and the $\text{CuNbTiB}_2\text{C}$ with nano-particles of Nb sintered at 650°C were attributed to their sufficient microstructures, which showed that there were no pores in them (Figure 2b, Figure 4b, Figure 3b, Figures 5b, 2a and 4a, respectively).

4. Conclusions

This study demonstrated the production of a novelty near-equiatomic multi-principal element alloy of $\text{Cu}_{40}\text{Nb}_{30}(\text{TiB}_2)_{20}\text{C}_{10}$ with both nano-particle- (14 nm) and micron-particle-sized ($\sim 44\mu\text{m}$) of Nb through the powder metallurgy route by using the spark plasma

sintering technique at two different sintered temperatures of 650 °C and 700 °C. After the fabrication of the alloys, an investigation was focused mainly on the following: Sintering mode, microstructures, microhardness, density, relative density, wear behavior, and corrosion properties in the H₂SO₄ acid environment. Based on the findings and discussion of the current study, it was discovered that the alloys with nano-particles of Nb sintered faster than any other alloys that were sintered. The microstructure of the alloy shows a dendritic configuration with the existence of graphite-rich and niobium-rich nano-segregations in the inter-dendritic areas. Furthermore, it was observed that the alloy of CuNbTiB₂ with nano-particles of Nb sintered at 650 °C recorded the highest microhardness value of 786.03 HV, while an alloy of CuNbTiB₂ with micro-particles of Nb sintered at 650 °C recorded the highest density and relative density of 7.806 g/cm³ and 96%, respectively. The alloy of CuNbTiB₂ with micro-particles of Nb sintered at 650 °C recorded the lowest coefficient of friction of 0.201. However, considering the wearing stability, the alloy that possesses the best wear stability as time progresses is an alloy of CuNbTiB₂ with nano-particles of Nb sintered at 700 °C. A safer wear behavior was disclosed by the alloy that maintained a stable friction coefficient as time goes on. The alloy of CuNbTiB₂ with micro-particles of Nb sintered at 700 °C shows the best anti-corrosion behavior in an H₂SO₄ acid environment. However, the obtained results in this study showed that the produced novelty alloy is a promising high-performance engineering material that can be more important in the aerospace industry.

Author Contributions: A.A.E.: Conceptualization, methodology, writing—original draft. E.R.S.: Supervisor, validation, editorial. W.K.K.: Investigation. J.S.: Investigation. J.M.N.: Visualization. I.D.I.: Investigation. All authors have read and agreed to the published version of the manuscript.

Funding: Department of science and technology (DST), South Africa.

Data Availability Statement: Not applicable.

Acknowledgments: The authors acknowledge Tshwane University of Technology and the department of science and technology (DST) South Africa for financial support.

Conflicts of Interest: The authors proclaimed that they have no known contending financial interests or personal relationships that could have appeared to affect the work delineated in this paper.

References

1. Jia, Z.; Nomoto, K.; Wang, Q.; Kong, C.; Sun, L.; Zhang, L.; Liang, S.; Lu, J.; Kruzic, J.J. A self-supported high-entropy metallic glass with a nanosponge architecture for efficient hydrogen evolution under alkaline and acidic conditions. *Adv. Funct. Mater.* **2021**, *31*, 2101586. [[CrossRef](#)]
2. Jia, Z.; Yang, T.; Sun, L.; Zhao, Y.; Li, W.; Luan, J.; Lyu, F.; Zhang, L.C.; Kruzic, J.J.; Kai, J.J.; et al. A novel multinary intermetallic as an active electrocatalyst for hydrogen evolution. *Adv. Mater.* **2020**, *32*, 2000385. [[CrossRef](#)] [[PubMed](#)]
3. Li, C.; Ferry, M.; Kruzic, J.J.; Li, X. Review: Multi-principal element alloys by additive manufacturing. *J. Mater. Sci.* **2022**, *57*, 9903–9935. [[CrossRef](#)]
4. Padture, N.P.; Gell, M.; Jordan, E.H. Thermal barrier coatings for gas-turbine engine applications. *Science* **2002**, *296*, 280–284. [[CrossRef](#)]
5. Praveen, S.; Kim, H.S. High-entropy alloys: Potential candidates for high-temperature applications—An overview. *Adv. Eng. Mater.* **2018**, *20*, 1700645. [[CrossRef](#)]
6. Tsao, T.-K.; Yeh, A.-C.; Kuo, C.-M.; Kakehi, K.; Murakami, H.; Yeh, J.-W.; Jian, S.-R. The high temperature tensile and creep behaviors of high entropy superalloy. *Sci. Rep.* **2017**, *7*, 12658. [[CrossRef](#)]
7. Yan, X.; Zhang, Y. Functional properties and promising applications of high entropy alloys. *Scr. Mater.* **2020**, *187*, 188–193. [[CrossRef](#)]
8. Yeh, J.-W.; Lin, S.-J. Breakthrough applications of high-entropy materials. *J. Mater. Res.* **2018**, *33*, 3129–3137. [[CrossRef](#)]
9. Romero, R.A.; Xu, S.; Jian, W.-R.; Beyerlein, I.J.; Ramana, C. Atomistic simulations of the local slip resistances in four refractory multi-principal element alloys. *Int. J. Plast.* **2022**, *149*, 103157. [[CrossRef](#)]
10. Cantor, B.; Chang, I.T.H.; Knight, P.; Vincent, A.J.B. Microstructural development in equiatomic multicomponent alloys. *Mater. Sci. Eng. A* **2004**, *375*, 213–218. [[CrossRef](#)]
11. Yeh, J.-W.; Chen, S.K.; Lin, S.-J.; Gan, J.-Y.; Chin, T.-S.; Shun, T.-T.; Tsau, C.-H.; Chang, S.-Y. Nanostructured high-entropy alloys with multiple principal elements: Novel alloy design concepts and outcomes. *Adv. Eng. Mater.* **2004**, *6*, 299–303. [[CrossRef](#)]

12. Senkov, O.N.; Wilks, G.B.; Miracle, D.B.; Chuang, C.P.; Liaw, P.K. Refractory high-entropy alloys. *Intermetallics* **2010**, *18*, 1758–1765. [[CrossRef](#)]
13. Wadsworth, J.; Nieh, T.; Stephens, J. Recent advances in aerospace refractory metal alloys. *Int. Mater. Rev.* **1988**, *33*, 131–150. [[CrossRef](#)]
14. Choudhary, S.; O'Brien, S.; Qiu, Y.; Thomas, S.; Gupta, R.; Birbilis, N. On the dynamic passivity and corrosion resistance of a low cost and low density multi-principal-element alloy produced via commodity metals. *Electrochem. Commun.* **2021**, *125*, 106989. [[CrossRef](#)]
15. Qiu, Y.; Thomas, S.; Gibson, M.A.; Fraser, H.L.; Birbilis, N. Corrosion of high entropy alloys. *npj Mater. Degrad.* **2017**, *1*, 15. [[CrossRef](#)]
16. Shi, Y.; Yang, B.; Liaw, P.K. Corrosion-resistant high-entropy alloys: A review. *Metals* **2017**, *7*, 43. [[CrossRef](#)]
17. Huang, C.; Tang, Y.-Z.; Zhang, Y.-Z.; Dong, A.-P.; Tu, J.; Chai, L.-J.; Zhou, Z.-M. Microstructure and dry sliding wear behavior of laser clad AlCrNiSiTi multi-principal element alloy coatings. *Rare Met.* **2017**, *36*, 562–568. [[CrossRef](#)]
18. Goh, G.D.; Agarwala, S.; Goh, G.L.; Dikshit, V.; Sing, S.L.; Yeong, W.Y. Additive manufacturing in unmanned aerial vehicles (UAVs): Challenges and potential. *Aerosp. Sci. Technol.* **2017**, *63*, 140–151. [[CrossRef](#)]
19. Diouf, S.; Molinari, A. Densification mechanisms in spark plasma sintering: Effect of particle size and pressure. *Powder Technol.* **2012**, *221*, 220–227. [[CrossRef](#)]
20. Guillon, O.; Gonzalez-Julian, J.; Dargatz, B.; Kessel, T.; Schierning, G.; Räthel, J.; Herrmann, M. Field-assisted sintering technology/spark plasma sintering: Mechanisms, materials, and technology developments. *Adv. Eng. Mater.* **2014**, *16*, 830–849. [[CrossRef](#)]
21. Matizamhuka, W. Spark plasma sintering (SPS)-an advanced sintering technique for structural nanocomposite materials. *J. South. Afr. Inst. Min. Metall.* **2016**, *116*, 1171–1180. [[CrossRef](#)]
22. Yousif, B. Design of newly fabricated tribological machine for wear and frictional experiments under dry/wet condition. *Mater. Des.* **2013**, *48*, 2–13. [[CrossRef](#)]
23. Kato, K. Wear in relation to friction—A review. *Wear* **2000**, *241*, 151–157. [[CrossRef](#)]
24. Alotaibi, J.; Yousif, B.; Yusaf, T. Wear behaviour and mechanism of different metals sliding against stainless steel counterface. *Proc. Inst. Mech. Eng. Part J J. Eng. Tribol.* **2014**, *228*, 692–704. [[CrossRef](#)]
25. Česánek, Z.; Schubert, J. Potentiodynamic evaluation of corrosion resistant coatings. *Metal* **2014**, 2014.
26. Alaneme, K.K.; Olubambi, P.A. Corrosion and wear behaviour of rice husk ash—Alumina reinforced Al–Mg–Si alloy matrix hybrid composites. *J. Mater. Res. Technol.* **2013**, *2*, 188–194. [[CrossRef](#)]
27. Mishra, A.; Balasubramaniam, R.; Tiwari, S. Corrosion inhibition of 6061-SiC by rare earth chlorides. *Anti-Corrosion Methods Mater.* **2007**, *54*, 37–46. [[CrossRef](#)]